

Photoemission study of amorphous carbon modifications and comparison with calculated densities of states

J. Schäfer, J. Ristein, R. Graupner, and L. Ley

Institut für Technische Physik, Universität Erlangen, Erwin-Rommel-Straße 1, 91058 Erlangen, Germany

U. Stephan and Th. Frauenheim

Institut für Theoretische Physik, Technische Universität Chemnitz, P.O. Box 964, 09107 Chemnitz, Germany

V. S. Veerasamy and G. A. J. Amaratunga

Department of Engineering, University of Cambridge, Cambridge, United Kingdom

M. Weiler and H. Ehrhardt

Fachbereich Physik, Universität Kaiserslautern, 67663 Kaiserslautern, Germany

(Received 14 July 1995)

In this study we present photoemission data for three different types of amorphous carbon modifications (*a*-C:H, *ta*-C:H, and *ta*-C) that owe their properties to their different preparations by radio frequency plasma, plasma beam, or arc discharge. Their properties are investigated by means of their characteristic plasmon loss following the C 1s core level, the core-level shape itself, and by their valence bands. For all three amorphous modifications as well as for the two crystalline ones, diamond and graphite, we present density of states calculations which in the amorphous case are based on molecular-dynamics simulations. The electronic density of states is fitted to the data using photoemission cross sections and a model for the lifetime broadening. The agreement achieved is very good and confirms the validity of the predicted structures that do not possess any significant larger π clusters.

I. INTRODUCTION

In this work we try to come to a realistic model of the three presently most interesting amorphous carbon materials, which owe their different properties to different deposition processes. The fundamental construction elements of amorphous carbon are sp^3 and sp^2 hybridized carbon atoms. The two natural crystalline modifications where either sp^3 and sp^2 hybridization occurs exclusively are diamond and graphite, respectively. Graphite is thermodynamically the most stable configuration, yet diamond lies only 2.9 kJ/mol (30 meV/atom) higher in energy and separated by an activation barrier.¹ These two crystals must form the basis of any analysis of an amorphous network. Notably the possibility of sp^2 hybridization makes this task so much more difficult than a comparison between, e.g., crystalline and amorphous silicon or germanium which occur in tetrahedral coordination only.

The amorphous carbon modifications contain, like *a*-Si:H, considerable amounts of hydrogen if they are prepared from a hydrocarbon plasma, as is the case for the classical parallel-plane radio-frequency (RF) plasma,² and the more recent technique of RF plasma beam deposition.³ The amount of bonded hydrogen is certainly one parameter which influences the structure and the electronic properties of the various forms of amorphous carbon.

The amorphous carbon material best analyzed to date is that deposited from an RF plasma of methane. Its atomic arrangement, expressed by the radial distribution function, has been probed by electron⁴ and neutron diffraction,^{5,6} and the microscopic density was obtained from the plasmon en-

ergies as measured by electron energy-loss spectroscopy (EELS).⁷ Concerning information about the types of bonds realized in the amorphous network, nuclear magnetic resonance spectroscopy^{8,9} has so far provided the most reliable sp^2/sp^3 ratios, while hydrogen bonding configurations have been studied by infrared (IR) absorption.¹⁰ Knowledge about defects stems from conductivity measurements,¹¹ electron spin resonance,¹² photoluminescence¹³ and photoelectron yield spectroscopy.¹⁴ It is the main objective of the present paper to provide, by means of photoelectron spectroscopy, information on the densities of states (DOS) of these materials and to see by comparison with pertinent model calculations to what extent structural aspects and differences in sp^2/sp^3 ratio are reflected in the DOS. These investigations extend earlier measurements of the valence-band spectra of amorphous carbon.^{15,16}

To this end we compare valence-band spectra obtained by x-ray excited photoelectron spectroscopy (XPS) after due correction for photoemission cross sections and final state effects with calculated densities of states. The calculations were performed for various model structures of amorphous carbon that were obtained via a molecular-dynamics approach described below. This procedure is first tested using the two crystalline modifications of carbon, diamond, and graphite.

The analysis of the valence-band spectra is augmented by that of the loss structure following the C 1s core line and by a brief discussion of the C 1s core line itself.

After the experimental part described in the next section, the results obtained are presented and discussed in three main parts. We first present the C 1s photoelectron loss spec-

tra in Sec. III before turning to the valence bands in Sec. IV. The trends observed in the valence bands together with their calculated densities of states are complemented in Sec. V by the shape of the C 1s line measured in high resolution. The conclusions for the amorphous carbon bonding are summarized in Sec. VI.

II. EXPERIMENT

A. Sample preparation

The basis of the present analysis are amorphous carbon samples prepared in fundamentally different deposition systems. The radio-frequency plasma decomposition of hydrides is the conventional technique for the deposition of amorphous semiconductors, while the two other techniques are especially developed to produce relatively hard amorphous carbon films with low content of sp^2 bonding. As the purpose of the present study is to compare films made by these three different techniques—rather than to discuss variations within a particular technique—the films were made under typical conditions that produce the “best” film for each deposition method as regards high hardness and mass density. The crystalline samples were highly oriented pyrolytic graphite (HOPG), and a type-IIB natural diamond heated up to 800 °C *in vacuo*.

The samples labeled *a*-C:H in the following were deposited from methane in a capacitively coupled parallel-plate RF plasma chemical-vapor-deposition (CVD) system at a flow rate of 3 sccm and a pressure of 0.10 mbar. The sample substrate was placed on the powered electrode which attained a self-bias of -200 V under the deposition conditions. Deposition was performed nominally at room temperature, but the substrate electrode was not actively cooled. The deposition mechanism is mainly due to radical reactions at the growth surface under the ion bombardment affected by the self-bias. Only this provides a suppression of polymerization and a cross linking of the amorphous network and thus enhances the density and the hardness of the growing film. The *a*-C:H samples so obtained have a rather low mass density of around 2 g cm^{-3} , a hydrogen content of typically 40 at. %, and are more sp^3 than sp^2 bonded.²

A different growth regime is obtained when the substrate is removed from direct contact with the plasma and the amorphous carbon is solely deposited from C- and H-containing ions such as C_2H_2^+ of well-defined energy. This so-called plasma beam deposition³ yields specimens with low hydrogen content (~ 25 at. %), high density, and a high fraction ($\sim 70\%$) of sp^3 -coordinated carbon atoms, which in turn are responsible for the considerable hardness of up to 61 GPa of this material.³ The samples investigated here were deposited with an ion energy of 104 eV per C atom from an acetylene plasma and they are referred to as tetrahedral hydrogenated amorphous carbon (*ta*-C:H) in what follows.

A modification of amorphous carbon that comes in its properties such as density (3.0 g cm^{-3}) and hardness (60–65 GPa) (Ref. 17) closest to diamond is hydrogen-free *ta*-C.^{18–21} It is deposited from an energy-selected C^+ -ion beam which is extracted from an arc plasma burning towards a high purity graphite target. We shall refer to these samples

TABLE I. Structural parameters of the three amorphous carbon samples as determined experimentally (upper part) and as used as input parameters in, or resulting from, the molecular-dynamics calculation (lower part).

| | <i>ta</i> -C | <i>ta</i> -C:H | <i>a</i> -C:H |
|--|-------------------|-------------------|-------------------|
| [H] (at. %) | 0 | 25 ^a | 40 ^b |
| ρ (g cm^{-3}) ^c | 2.68 | 2.20 | 1.70 |
| ρ (g cm^{-3}) ^d | 2.75 | 2.7 | |
| $[sp^3]/([sp^3]+[sp^2])$ | 0.65 ^e | 0.65 ^e | 0.63 ^f |
| [H] (at. %) | 0 | 20 | 39 |
| ρ (g cm^{-3}) | 3.0 | 3.0 | 2.2 |
| $[sp^3]/([sp^3]+[sp^2])$ | 61 | 67 | 39 |

^aFrom ^{15}N method (Refs. 25 and 24).

^bEstimated from IR absorption and comparison with literature data (Refs. 2 and 8).

^cFrom plasmon energies of the C 1s photoelectron loss spectra (this work).

^dFrom high-energy transmission EELS on *ta*-C (Refs. 18 and 19) and *ta*-C:H (Refs. 25 and 24).

^eFrom *K*-edge EELS (Refs. 25 and 18).

^fFrom UPS valence-band spectra (Ref. 16) and see text.

which were deposited from 50-eV ions as *ta*-C. Structural properties of all three *a*-C modifications are gathered in Table I.

B. Photoelectron spectroscopy

The core and valence-band photoemission (PE) spectra were measured using monochromatized Al K_α radiation ($h\nu = 1486.6$ eV) at a pass energy of 25 eV, resulting in an experimental resolution of 0.5 eV. Calibration of the binding energy axis to the Fermi level was performed by measuring the Fermi edge of a gold sample under an identical setting of the spectrometer. The graphite sample which was cleaved in the preparation chamber under a flow of dry nitrogen and the *a*-C:H specimen which could be transferred under ultrahigh vacuum from the deposition system into the PE spectrometer showed no sign of contamination. The other samples which were prepared *ex situ* exhibit an oxygen-containing surface contamination. It was measured as a few atomic percent from the O 1s/C 1s intensity ratio. The oxygen is, however, not bound to carbon since no chemically shifted C 1s component was detected. The O 2p signal did, nevertheless, interfere with the valence-band spectra as indicated by the feature around 26-eV binding energy in Fig. 1. Since the O 2s peak just scaled with the superficial oxygen concentration and did not otherwise affect the remainder of the spectra, we corrected for this contribution as indicated in Fig. 1 rather than attempting to remove the contamination through Ar-ion bombardment, which would have affected the atomic structure of the surface layer (~ 30 Å) probed by XPS. The O 2p electrons at ~ 6 -eV binding energy give no measurable contribution to the spectra because their cross section is 7.3 times smaller.²²

III. CORE-LEVEL LOSS SPECTRA

The C 1s line at ~ 285 -eV binding energy is followed by a structured background of electrons extending towards

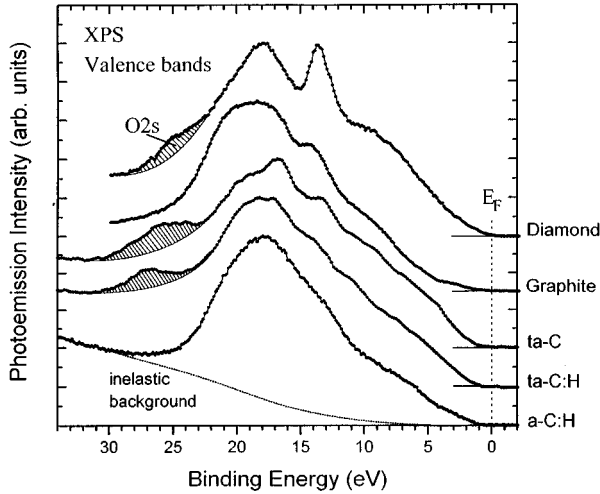


FIG. 1. X-ray photoelectron (XP) spectra of the valence bands of all three amorphous carbon modifications. For comparison, the two crystalline modifications in the form of HOPG and diamond, (111) surface, are shown. The raw data carry an inelastic tail which can be fitted via the loss function derived from the C 1s photoelectron energy-loss spectra (exemplary shown for *a-C:H*). For the further analysis of the spectra [Figs. 5(a) and 7(a)] the inelastic background and the contribution of the O 2s electrons around 26 eV due to oxygen contaminants were subtracted as indicated.

higher binding (lower kinetic) energies (see Fig. 2). The so-called loss spectrum corresponds to C 1s photoelectrons which have suffered energy losses on the way from their point of creation to the sample surface and it is thus characteristic for the sample under investigation. Because the main loss mechanism for high-energy electrons is the creation of bulk plasmons, the energy $\hbar\omega_{\max}$ of the maximum in the loss spectrum is commonly identified with the plasmon energy $\hbar\omega_p$. Under the further assumption that $\hbar\omega_p$ is related to the valence electron density n_e as in a free-electron metal, $\omega_p^2 = \omega_{p,0}^2 = n_e e^2 / (m\epsilon_0)$, the mass density of the sample can be calculated from $\hbar\omega_{\max}$ and the known number of valence electrons per atom. This is, however, incorrect because neither form of carbon is a free-electron metal nor does $\hbar\omega_{\max}$ correspond to the plasmon energy. This is because electrons can suffer multiple losses and the loss spectrum $S(E)$ is a superposition of partial loss spectra $S_i(E)$,

$$S(E) = \sum_{i=1}^{\infty} S_i(E), \quad (1)$$

where S_i is the kinetic-energy distribution of photoelectrons that have suffered i losses before leaving the solid. The differential inelastic scattering probability (per unit path length) for an energy loss $\hbar\omega$ is given by $\lambda_e^{-1}G(\hbar\omega)$, where $G(\hbar\omega)$ is the normalized loss function,

$$G(\hbar\omega) = \text{Im}\{-1/\epsilon(\hbar\omega)\} / \int_0^{\infty} \text{Im}\{-1/\epsilon(\hbar\omega)\} d\hbar\omega, \quad (2)$$

λ_e is the inelastic scattering length, and $\epsilon(\hbar\omega)$ is the complex dielectric function of the material. For a homogeneous material the probability of multiple losses obeys Poisson's

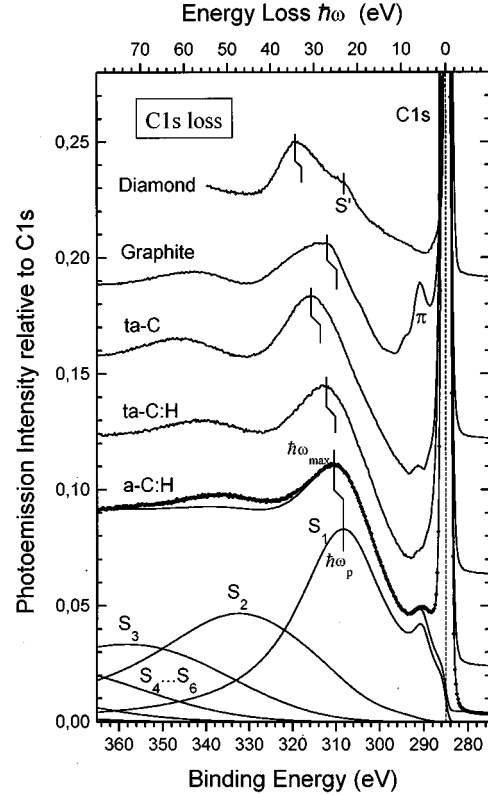


FIG. 2. C 1s photoelectron energy-loss spectra for all carbon samples investigated. Diamond has its maximum at the highest loss energy; it also bears a surface plasmon (S) at a reduced energy. Graphite and, less pronounced, the three amorphous samples reveal also the characteristic π plasmons as discussed in the text. For *a-C:H* also the deconvolution procedure to extract the loss function from the spectra is illustrated by the partial loss spectra S_1, \dots, S_6 . Since the elastic line $S_0(E)$ is almost a δ function with respect to the structures of the loss spectrum, $S_1(\Delta E)$ is to a very good approximation identical to the loss function $G(\Delta E)$.

statistics and after integration over the exponential excitation profile of the photoelectrons with a decay constant λ_p a recursion formula for the S_i results,

$$S_{i+1}(E) = \frac{\lambda_p}{\lambda_e + \lambda_p} \int_0^{\infty} G(\hbar\omega) S_i(E + \hbar\omega) d\hbar\omega, \quad (3)$$

with $S_0(E)$ the primary spectrum of electrons as a function of kinetic energy E .²³ Equation (3) just expresses the fact that each partial loss spectrum results from its predecessor by convolution of the latter with the function $G(\hbar\omega)$. The factor $\lambda_p / (\lambda_e + \lambda_p) < 1$ expresses the geometrically decreasing probability of electrons to escape from the sample with each scattering event. The loss function $\text{Im}\{-1/\epsilon(\omega)\}$ was parametrized by a superposition of two asymmetrical Lorentzians, one centered at $\hbar\omega_p$ corresponding to the bulk plasmon around 26 eV, and the other to the so-called π plasmon at 6 eV. We made the additional provision that the relative amplitude of S_1/S_0 was enhanced by a factor t over the ratio $\lambda_p / (\lambda_e + \lambda_p)$ to account for intrinsic plasmon creation²³ and found $t=1.2$ for diamond and $t=1.7 \pm 0.1$ for all other samples. A reasonable fit of the total loss spectra could be obtained as demonstrated in Fig. 2 for the case of *a-C:H*.

From the best parametrization of the loss function its characteristic peak energy was obtained directly. As can be seen in Fig. 2, $\hbar\omega_p$ differs by ~ 2 eV from $\hbar\omega_{\max}$ in *a*-C:H and the differences in the other samples are comparable.

The difference between $\hbar\omega_p$ and the equivalent free-electron plasmon energy $\hbar\omega_{p,o}$ amounts to 3.3 eV in diamond ($\hbar\omega_p = 34.5$ eV, $\hbar\omega_{p,o} = 31.2$ eV) and 1 eV in graphite ($\hbar\omega_p = 26.0$ eV, $\hbar\omega_{p,o} = 25.0$ eV). Using these two elements as standards we have determined the electron and thus also the mass densities of the other carbon modifications by interpolating on the linear $\hbar\omega_p$ vs n_e^2 curve defined by graphite and diamond. The results are gathered in Table I.

For the hydrogen-containing carbon modifications the contribution of the H atoms (one valence electron) to the electron density has to be taken into account when converting n_e to mass density. We have done so using a hydrogen content of 25 at. % for *ta*-C:H and 40 at. % for *a*-C:H. Despite a rather large uncertainty in these concentrations ($\sim \pm 20\%$) the uncertainty in ρ derived therefrom is negligible due to the small mass ratio of H to C. For *ta*-C and *ta*-C:H which were prepared *ex situ*, the plasmon energy did not seem to be a purely intrinsic property of the samples but was instead found to be decreasing with increasing oxygen contamination of the surface. The reason for this correlation is unclear so far. It appears, however, that oxygen contamination does affect the loss spectrum. The densities extracted for the least contaminated samples whose loss spectra are shown in Fig. 2 serve therefore as lower limits. Transmission EELS which does not suffer from surface contamination has been performed on *ta*-C and *ta*-C:H samples deposited under identical conditions as the samples we investigated. The mass densities obtained from those experiments are also shown in Table I.

Also listed in Table I are the hydrogen content^{2,8,24} and the fraction of C atoms that are sp^3 hybridized. The values of 70% for this fraction in *ta*-C and *ta*-C:H were obtained from the ratio of C $1s \rightarrow \sigma^*$ to C $1s \rightarrow \pi^*$ transitions in high-energy EELS spectra.^{18,25} A relative sp^3 content of 62% has been estimated for *a*-C:H sample from an analysis of the ultraviolet photoemission spectroscopy valence-band spectra.¹⁶ In that analysis the contribution of the H $1s$ electrons to the spectrum was neglected. Taking this contribution into account reduces the sp^3 content to 56%.²⁶

Besides the main peak in the loss functions of Fig. 2, a second structure at 6 eV is visible which is usually ascribed to the π electrons of the material. The presence of this structure is thus a clear indication of sp^2 -bonded C atoms in a graphitic environment or of double bonds. It is, however, not possible to derive the sp^2 fraction from the ratio of π to $(\sigma + \pi)$ plasmons for reasons that have been discussed at length by Taft and Philipp²⁷ and by Daniels *et al.*²⁸ It should be noted that the crystalline diamond surface is the only one which shows a loss feature compatible with a surface plasmon. Those surface plasmons are expected at a $\sqrt{2}$ times smaller loss energy than the corresponding bulk plasmons and they occur only at perfectly clean and sufficiently flat surfaces.²⁹ We never observed a surface plasmon by photoelectron energy-loss spectroscopy on an amorphous semiconductor sample, either in *a*-Si:H or any amorphous silicon alloy, or in any form of amorphous carbon. Even on the most

perfect, hydrogen-saturated crystalline Si(111) surfaces, we never saw a comparably strong surface plasmon as in diamond. The identification of the diamond loss structure at 23 eV as the surface plasmon of diamond follows the conventional interpretation,³⁰ but is only based on the ratio of $\omega_p/\omega_{s'} = 1.47 \approx \sqrt{2}$ which could, of course, be also coincidental and S' be rather due to specific interband transitions in diamond. Considering the rather poor quality of polished diamond surfaces,³¹ this might even be the more likely interpretation. The possibility of surface plasmons at semiconductors is still an open question; however, it is beyond the scope of this paper.

Finally, we used the differential scattering probability $\lambda_e^{-1}G(E)$ as obtained from a fit to the C $1s$ core-level losses to correct for the inelastic contribution to the respective valence-band spectra as indicated for *a*-C:H in Fig. 1. The multiple convolution method to obtain the total spectrum of inelastic electrons $S(E)$ via the recursion formula of Eq. (3) is mathematically equivalent to an integral equation,

$$S(E_B) = \frac{\lambda_p}{\lambda_p + \lambda_e} \int_{-\infty}^{E_B} \{ (1-t)S(E') + tI(E') \} G(E_B - E') dE', \quad (4)$$

where $I(E_B)$ is the experimentally observed spectrum of elastic *and* inelastic electrons. Here t is again the enhancement factor for the first plasmon loss, which accounts for the intrinsic plasmons. Although (4) is an implicit equation for $S(E_B)$, it can be numerically integrated starting from the low-binding-energy end of the spectrum where $S(E_B)$ is known to be zero. We used Eq. (4) with the very same parameters as obtained from the C $1s$ losses and just had to allow a variation of t within 10% [to let $S(E_B)$ merge smoothly with $I(E_B)$ at high binding energies].

IV. VALENCE BANDS AND DENSITIES OF STATES

A. Molecular-dynamics calculation

In this subsection we give a brief description of the molecular-dynamics (MD) method used to model the amorphous carbon structures theoretically. Details of the technique have already been published elsewhere³²⁻³⁴ and are not the subject of this paper.

Within the Born-Oppenheimer approximation, the interatomic forces are calculated in an MD density-functional approach. Simulated annealing, based on an accurate calculation of the total structure energy as a function of all atom coordinates, requires Newton's equation of motion for all atoms arranged in a three-dimensional periodic supercell structure to be solved and then integrated numerically. The procedure should ultimately lead to a stable minimal-energy configuration.

As a starting point the effective one-electron potentials are calculated together with the electronic wave functions for a single atom in the local-density approximation (LDA). These wave functions can be used as a minimal basis for the LCAO (linear combination of atomic orbitals) ansatz for expanding the Kohn-Sham orbitals, which then transforms the Kohn-Sham equations into a set of algebraic equations. Diagonalization leads to the cluster orbital eigenenergies and

eigenfunctions. The cohesive energy of the structure can then be written as the sum of two parts,

$$E_{\text{tot}} = \sum_j n_i \varepsilon_i(\{\mathbf{R}_l\}) + \sum_i \sum_{<k} V_{\text{rep}}(\{\mathbf{R}_l - \mathbf{R}_k\}), \quad (5)$$

where the first term is the summation over all cluster orbital energies ε_i with occupation n_i taking into account the intra-atomic electron-electron interaction through the self-consistent LDA calculation. The second term E_{rep} represents a short-range repulsive energy from core-core and electron-electron interactions at different lattice sites. For computing time reasons a fitted potential curve is used for the latter.³²

Finally, the interatomic forces can be calculated from the gradients of the total energy at all atom sites: $\mathbf{F}_l = -\partial E_{\text{tot}}/\partial \mathbf{R}_l$. The equations of motion can then be solved by numerical integration. The simulated annealing starts with an equilibration of a random hard-sphere gas at 8000 to 10000 K for 10^{-13} sec using a time step of 8×10^{-16} sec for *ta*-C and 2×10^{-16} sec for *ta*-C:H and *a*-C:H, after which the structure is quenched at a cooling rate of 10^{16} K/sec, followed by a final equilibration of the structure at room temperature for 10^{-13} sec. The structures were generated for a fixed hydrogen content and a given mass density in a periodically arranged supercell containing 128 carbon atoms plus the relevant number of hydrogen atoms. Once the physical structure with its atom positions is solved, the electronic density of states is known as well and the partial densities of states have been calculated. The band structures and DOS of diamond and graphite were calculated using the recursion method within the same LCAO scheme,³⁴ whereas the DOS of the amorphous systems were obtained by means of a Gaussian smoothing of the eigenvalue spectrum at the Γ point of the Brillouin zone of the super cell. The densities and hydrogen concentrations that were used to model the four *a*-C modifications to be discussed here are given in Table I, as are the resulting *sp*³ ratios.

The value that resulted from the molecular-dynamics calculation (39%) is still considerably lower, which is not sufficiently explained with the slightly higher density (2.0 g cm^{-3} instead of 1.7 g cm^{-3}) used as an input parameter. It rather appears that for the low-density material *a*-C:H the simulated annealing cannot model the deposition process as well as it does for the two ion-beam-deposited materials. This is due to MD not taking into account chemical effects, which are important when using CH_x^+ radicals of relatively low energy. However, although the model to be discussed here yielded somewhat different structural properties for the *a*-C:H sample as compared to the experimental values, the characteristic differences in the electronic density of states as compared to the tetrahedrally coordinated *ta*-C and *ta*-C:H samples are described surprisingly well (see Sec. IV C).

B. Fitting to XPS: Matrix elements and lifetime

As mentioned earlier, the aim of the present study is to compare the electronic structure of different *a*-C modifications with the results of molecular-dynamics calculations. The electronic structures are determined through XPS valence-band spectra which are closely related to the occu-

ried density of states. In crystalline materials the DOS is governed by pronounced structures related to van Hove singularities in the underlying band structure and its suffices usually to compare the energies of these structures in theory and experiment. In amorphous materials the concept of van Hove singularities loses its meaning and structures in the DOS are usually somewhat more poorly defined than in crystalline materials. This means that any comparison between theory and experiment requires that they be treated in such a way that their results resemble each other as closely as possible.

The main differences between an XPS valence-band spectrum and a DOS are (i) the photoemission cross section, which may vary throughout the DOS on account of the different atomic origin contributing to the DOS, and (ii) the imaginary part of the hole self-energy or equivalently the broadening of spectral features due to the finite lifetime of the hole left behind after the photoexcitation process. The bulk of the corresponding real part, the relaxation energy, is automatically taken into account by referring experiment and theory to a common reference energy, the Fermi level E_F in our case.

The spectral dependence of the lifetime broadening and the specific atomic photoelectron cross sections for *s* and *p* states (see below) should be the same for both crystalline and amorphous manifestations of solid carbon. Consequently, we will determine both contributions by adjusting the densities of states of diamond and graphite to their respective XPS valence-band spectra. In doing so we assume that the values for the lifetime broadening and the photoemission cross section can be carried over to the DOS of the amorphous modifications.

The photoemission cross section that varies throughout the valence bands is taken into account by separating the DOS into their C 2*s*, C 2*p*, and H 1*s* components in the form of partial densities of states (PDOS) and multiplying each by its proper photoemission cross section σ . As a first approximation, the corresponding free atom cross sections as calculated by Scofield³⁵ and Yeh²² have been used.

The comparison of the XPS spectra of graphite with the partial density of states, however, revealed that for a good fit a difference in photoelectron cross section of a factor of 2 had also to be assumed between the C 2*p* orbitals participating in σ bonds and those forming π bonds. Consequently, H 1*s*, C 2*s*, C 2*p* _{σ} , and C 2*p* _{π} partial densities of states were evaluated for all structures and weighted with the appropriate photoelectron cross sections in order to fit the XPS valence-band spectral $I(E)$:

$$I(E) \propto \sigma_{\text{C}2s} D_{\text{C}2s}(E) + \sigma_{\text{C}2p_\sigma} D_{\text{C}2p_\sigma}(E) + \sigma_{\text{C}2p_\pi} D_{\text{C}2p_\pi}(E) + \sigma_{\text{H}1s} D_{\text{H}1s}(E). \quad (6)$$

For the cross-section ratio $\sigma_{\text{C}2s}/\sigma_{\text{C}2p_\sigma}$ for x-ray photoemission with $\hbar\omega = 1486.6 \text{ eV}$, Gelius obtained a value of 13.³⁶ This value is based on a spectrum of methane using gross atomic populations obtained from *ab initio* calculations with 2*p* polarization functions on the hydrogen atoms. We found this experimentally based cross section more realistic than the theoretical value of 32 calculated by Scofield³⁵ and

Yeh,²² a discrepancy of a more systematic nature for some elements as noted by Scofield. The C 2*s* wave function with its one node varies more rapidly compared with the nodeless C 2*p* function and hence has a stronger cross section. The same argument but even more pronounced is valid for H 1*s* that we have to deal with in hydrogenated amorphous carbon. The calculated value for atomic hydrogen^{35,22} is $\sigma(\text{C}2s)/\sigma(\text{H}1s)=240$. This means that hydrogen is practically invisible in XPS and the hydrogen-derived partial density of states cannot be judged.

The second correction that has to be applied to the theoretical DOS is the lifetime broadening of the hole state. For the true many-electron system, the hole state is not a stationary state. It decays with a finite lifetime τ which gives rise to

$$\Gamma_h(E) = \hbar A \int_{E+E_g}^{E_V} \left\{ \int_{E_V-(E_2-E-E_g)}^{E_V} D(E_2)D(E_3)D(E_3+E_2-E)dE_3 \right\} dE_2, \quad (7)$$

where E is the initial state hole energy, E_V is the energy of the valence-band maximum (VBM), E_g is the gap energy, $D(E)$ is the one-electron density of states, and A is proportional to an average matrix element of the Coulomb interaction between the quasiparticles. Since we are interested in a variation of the lifetime broadening over the complete valence band, the density of states can be approximated with sufficient accuracy by step functions for the valence and conduction bands,

$$D(E) = D_V \Theta(E_V - E) + D_C \Theta(E - E_V - E_g). \quad (8)$$

Integration of Eq. (8) is then readily performed giving

$$\Gamma_h(E_B) \propto (E_B - E_{\text{VBM}} - E_g)^2 \Theta(E_B - E_{\text{VBM}} - E_g), \quad (9)$$

i.e., Γ_h increases quadratically with binding energy above a threshold equal to the gap energy relative to the VBM.

For diamond [Fig. 3(b)] with $E_g = 5.5$ eV we expect the threshold energy to be approximately 6.5 eV if referenced to E_F . In practice we found that placing the origin of the parabola slightly higher at 10-eV binding energy gives the best agreement between XPS and the DOS. We thus convoluted the calculated DOS with a Lorentzian with width $\Gamma = 0.035$ eV⁻¹($E_B - 10$ eV)² + 1.0 eV. From the work of Kane we extrapolate a hole lifetime broadening of ~ 1 eV at an energy 10 eV below E_V . The quadratic term in our fit reaches 1 eV at 12.6 eV below E_V . However, in addition to that, we found that an additional constant broadening of 1.0 eV is needed that cannot be explained by primary hole scattering. The reason for this additional contribution to the broadening is not yet understood.

For graphite, which is a semimetal due to the π states, we interestingly found that apart from a constant scattering term of 0.5 eV, the same threshold energy is required to calculate Γ in order to give the best agreement with the data. This observation points to a considerably lower scattering rate for holes into states within the π band as compared to states within the σ band. For amorphous carbon, a fixed threshold

a Lorentzian lifetime broadening of $\Gamma_n = \hbar/\tau$ width that contributes to the spectral function measured in photoemission. Also the photoelectron contributes in principle to the total lifetime broadening of photoemission resonances due to inelastic scattering on its way to the surface. This contribution, however, is negligible in the XPS regime of high excitation energy.³⁷ The leading mechanism responsible for Γ in a semiconductor is the pair production across the gap as discussed by Kane.³⁸ For a constant Coulomb interaction matrix element the hole scattering rate Γ is determined by the densities of final and initial states for the three quasiparticles involved: the initial hole at energy E , the second hole at energy E_2 , and the electron at E_3 , which are created in the scattering process:

energy of 10 eV and prefactor of 0.025 eV⁻¹ in Eq. (9) gave the best overall agreement. No constant contribution is required. This difference between the amorphous and crystalline structures might be due to the different methods by

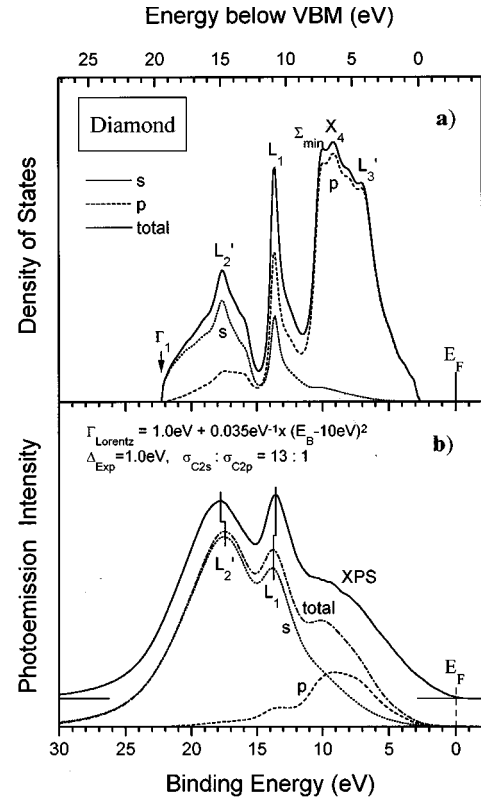


FIG. 3. (a) Calculated partial and total densities of states for diamond and (b) corresponding fit to the XP spectrum with the parameters listed in the figure. The position of the L_2' , and L_1 maxima from (a) are marked also in the simulation in (b) as well as the corresponding features in the XP spectrum. Note that the lower energy scale is referred to the Fermi level, in contrast to the values in Table II.

TABLE II. Theoretical and experimental band-structure data of diamond. Energies are referred to the valence-band maximum. The data of Fahy, Louie, and Cohen (Ref. 43) and Salehpour and Satpathy (Ref. 44) were extracted from density of states plots; all other theoretical data were found tabulated in the corresponding references with the exception of Σ_{\min} , which was in all cases taken from band-structure plots.

| | Γ'_1 | L'_2 | L_1 | Σ_{\min} | X_4 | L'_3 |
|----------------------------------|-------------|----------|----------|-----------------|-------|--------|
| Theory | | | | | | |
| Zunger and Freeman (Ref. 39) | 20.44 | 15.17 | 12.18 | | 6.09 | 2.82 |
| Bachelet ^a (Ref. 40) | 21.68 | 15.79 | 13.73 | 8.4 | 6.43 | 2.86 |
| Chelikowsky and Louie (Ref. 41) | 21.03 | 15.29 | 13.09 | 9.3 | 6.27 | 2.82 |
| Huang and Ching (Ref. 42) | 22.26 | 16.42 | 13.57 | 9.9 | 7.9 | 3.7 |
| Fahy, Louie, and Cohen (Ref. 43) | 21.7 | 15.7 | 11.3 | 8.1 | 6.0 | 3.3 |
| Salehpour and Satpathy (Ref. 44) | 21.5 | 15.5 | 11.2 | 8.7 | 6.1 | 3.1 |
| This work | 19.8 | 15.1 | 11.1 | 7.4 | 6.6 | 4.3 |
| Experiment | | | | | | |
| Himpsel ^a (Ref. 45) | 21.1 | 15.2 | 12.8 | | | |
| This work | | 15.2±0.2 | 11.1±0.2 | | | |

^aHamann-Schlüter-Chiang pseudopotential calculation with a basis of local orbitals. The same calculation with a plane-wave basis gives identical results within 0.25 eV.

^bFrom angular integrated photoemission.

which the DOS were extracted from the calculations. While for the amorphous structures the eigenvalue spectrum at the Γ point of the Brillouin zone was explicitly used and smoothed by a Gaussian, the DOS for diamond and graphite were obtained by the recursion method.³³ Although this method also contains an implicit smoothing, the structure might nevertheless come out sharper than in the case of the Gaussian smoothing of the eigenvalue spectrum.

In Fig. 3(a) the partial s and p as well as the total valence-band densities of states for diamond are shown as calculated by the same LCAO formalism used for the amorphous structures. van Hove singularities are labeled with the critical points in the band structure with which they are associated. In Fig. 3(b) we show a simulation of the XP spectrum (inelastic background subtracted) obtained on the basis of this calculation. The partial densities of states were broadened in the way described in the last section and weighted with their respective photoemission cross sections. The agreement in peak positions and relative intensities of the various peaks is rather good considering the severe approximations that were necessary for the evaluation of the photoemission cross section.

The L_1 and L'_2 maxima in the DOS are clearly resolved in the XP spectra with peak positions deviating by less than 0.3 eV from the values predicted by the calculation. We take this as an indication that the lowest two valence bands which essentially form the s partial density of states that dominates the XP spectra are fairly accurately reproduced by our calculation. Note that the amplitude of the peak at 13.7 eV is approximately the same as (or in the experimental spectrum even slightly larger than) that of the peak at 17.8 eV due to the large amplitude of the L_1 maximum in the DOS [Fig. 3(a)]. The Σ_{\min} , X_4 , and L'_3 maxima are weaker due to the predominant p character of the wave functions and are not resolved in the XP spectrum. Instead, a broad shoulder to lower binding energies appears at about 10 eV.

The critical point energies of diamond derived from the XPS analysis and our calculation are compared in Table II

with theoretical^{39–44} and experimental⁴⁵ results from the literature.

In Fig. 4(a) the calculated partial densities of states for graphite are shown in a similar manner as in Fig. 3(a) for diamond. Since we are interested mainly in the s -type density of states we restrict ourselves to a two-dimensional calculation and neglect interlayer interaction. Again the promi-

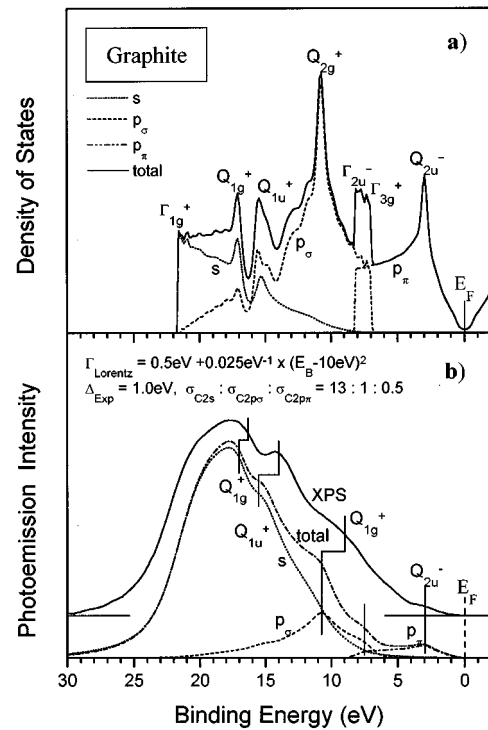


FIG. 4. (a) Calculated partial and total DOS for graphite and (b) corresponding fit to the XP spectrum with parameters listed in the figure. The positions of the Q_{1g}^+ , P_3^+ , Q_{2g}^+ , and Q_{2u}^- maxima of (b) along with the corresponding features in the XP spectrum. In contrast to diamond the calculation tends to overestimate the binding energies of the s and p_σ band. For details see text.

TABLE III. Theoretical and experimental band-structure data for graphite. When two bands were split at a certain point within the Brillouin zone we took the average value if they corresponded to a single peak in the DOS (Q_{1g}^+ , Q_{2u}^-) and the appropriate extreme value in case of a band extremum (Γ_{1g}^+ , Γ_{2u}^-). Energies are referred to the valence-band maximum, which in graphite is identical to the Fermi level. With the exception of Refs. 46 and 52 all theoretical data were extracted from band-structure plots.

| | Γ_{1g}^+ | Q_{1g}^+ | $P_3^+(Q_{1u}^+)$ | Q_{2g}^+ | Γ_{2u}^- | Γ_{3g}^+ | Q_{2u}^- |
|---|-----------------|------------|-------------------|------------|-----------------|-----------------|------------|
| | Theory | | | | | | |
| Willis, Fitton, and Painter (Ref. 49) | 22.0 | 15.4 | (13.5) | 8.0 | 8.0 | 4.9 | 2.0 |
| Zunger (Ref. 46) | 21.2 | 16.0 | (13.1) | 7.0 | 6.0 | 3.0 | 1.9 |
| Samuelson and Batra (Ref. 47) | 21.5 | 16.5 | 15.2 (16.0) | 9.7 | 8.0 | 6.4 | 2.3 |
| Tatar and Rabii (Ref. 50) | 19.3 | 14.7 | 13.5 (13.9) | 7.2 | 7.9 | 4.1 | 2.3 |
| Holzwarth ^a (Ref. 51) | 20.8 | 15.1 | 14.0 (14.7) | 7.2 | 9.1 | 3.4 | 2.7 |
| Holzwarth ^b (Ref. 51) | 21.5 | 16.1 | 14.2 (14.7) | 7.6 | 8.6 | 4.2 | 3.1 |
| Jansen and Freeman (Ref. 52) | 19.6 | | | | 8.7 | 4.6 | |
| Charlier, Gonze, and Michenaud (Ref. 48) | 20.0 | 14.7 | 12.9 (13.7) | 6.8 | 9.0 | 3.6 | 2.8 |
| This work | 21.7 | 17.0 | (15.5) | 10.7 | 8.2 | 6.9 | 2.9 |
| | Experiment | | | | | | |
| McFeely <i>et al.</i> ^c (Ref. 53) | | 18±1 | 13.8 | 8.1 | | | |
| Bianconi, Hagstrom, and Bachrach ^c (Ref. 54) | 22.5 | | (13.6) | 8 | 5.7 | 3.0 | |
| McGovern ^d (Ref. 55) | 20.6 | | | | 8.1 | 4.6 | 2.9 |
| Law, Barry, and Hughes ^d (Ref. 56) | | | | 8.0 | 8.5 | 5.5 | 2.8 |
| This work | | 16.5±0.5 | 14.0±0.5 | 9.0±0.5 | | | 3.0 |

^aHedin-Lundqvist exchange-correlation approximation.

^bSlater approximation.

^cFrom angular integrated photoemission.

^dFrom angular resolved photoemission.

ment peaks are labeled with the critical points in the band structure they are associated with, following the notation of Zunger.⁴⁶ The π band exhibits a sharp maximum at 3-eV binding energy and overlaps between 6.8 and 8.3 eV with the σ bands resulting in a second maximum in that range. The most prominent peak in the DOS at 10.7 eV corresponds to Q_{2g}^+ . All these features are predominantly of p -type character and only the last two peaks Q_{1u}^+ and Q_{1g}^+ appear clearly in the s -type partial DOS and are therefore expected to dominate the XPS spectrum. In more recent calculations, in which the interlayer interaction has been included, the band structure is presented in the three-dimensional Brillouin zone (BZ). For a comparison with two-dimensional calculations, one should note that the critical points L and M of the three-dimensional BZ are projected both onto Q in the two-dimensional case and K and H onto P . Since the dispersion of the valence bands is negligible along the \vec{c} axis (except for the π band), we used the band energies of K and M for a comparison with our results. Whereas the identification of the DOS peak at about 15 eV as Q_{1u}^+ in the two-dimensional calculations is unambiguous, things get more complicated in the three-dimensional case. We did not find any explicit assignment of a corresponding DOS peak to a critical point (neither to M which would be consistent with Q nor to K) in the literature. The only publications which contain three-dimensional band structure *and* DOS plots are by Samuelson and Batra⁴⁷ and by Charlier, Gonze, and Michenaud.⁴⁸ An analysis of their plots identifies their DOS maximum which

corresponds to our Q_{1u}^+ peak to be rather associated to the K point than to M . Thus it would correspond to P_3^+ in the two-dimensional notation and not to Q_{1u}^+ . The reason for this discrepancy between the two- and three-dimensional calculations is unclear so far. In the summary of literature data in Table III we have therefore listed both critical points in the vicinity of 14 eV, i.e., Q_{1u}^+ and P_3^+ , the difference being, however, 0.9 eV at most.

A major difference compared to diamond is seen at the bottom of the valence band and is due to the two-dimensional character of graphite: the DOS ends at ~ 22 -eV binding energy with a discontinuity, whereas for diamond a smooth decrease of the DOS is observed. This characteristic difference between both materials is indeed also reflected in the XP spectra. The spectrum of graphite ends with a much sharper cutoff at high binding energies as compared to diamond. The quantitative comparison between calculation and experiment, however, reveals considerably larger deviations compared to diamond. The two main features in the s -type partial DOS at 17.0 and 15.5 eV corresponding to Q_{1g}^+ and Q_{1u}^+ , respectively, are measured at 16.5 ± 0.5 eV and 13.6 ± 0.5 eV, respectively. The main peak in the p band corresponds to a shoulder in the XP spectrum at 9.0 ± 0.5 eV.

In Table III we have compiled our results for graphite along with more recent literature data from theory⁴⁶⁻⁵² and experiment.⁵³⁻⁵⁶ Our calculated positions for Q_{1u}^+ and Q_{2g}^+

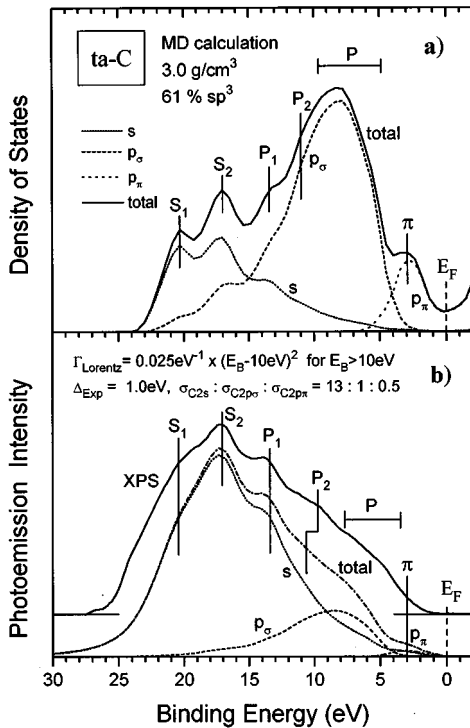


FIG. 5. (a) Partial and total DOS for tetrahedral amorphous carbon as obtained by simulated annealing molecular-dynamics calculation. The density of 3.0 g cm^{-3} was used as an input parameter; the resulting structure had an sp^3 content of 61%. (b) XP spectrum (background corrected) of a *ta-C* sample and fit to the partial DOS of (a). Characteristic features of the DOS which are reidentified in the XP spectrum are marked by bars. For details see text.

deviate from the literature data by about 2 eV and for Q_{1g}^+ by approximately 1 eV. The absence of the shoulder predicted at 7.5 eV, moreover, probably means that the π -band minimum (Γ_{2u}^-) is very close to or even at a higher binding energy than Q_{2g}^+ . Thus the separate peak at 7.5 eV in Fig. 4(a) is artificial probably as a consequence of the neglect of interlayer interaction which broadens the π band. This interpretation is supported by the majority of the literature data in Table III. The π band, finally, is fairly well reproduced with respect to its peak position at 3.0 eV. However, also in this case its separation from the σ bands is much more pronounced than in the XP spectrum. Obviously, the energy difference between Γ_{3g}^+ and Q_{2u}^- (4.0 eV) is overestimated by the calculation, which is again confirmed by the literature data (0.7–2.9 eV with the exception of Ref. 49 at 4.1 eV; see Table III).

It should be mentioned that the DOS calculation of graphite has meanwhile been improved using a modified set of parameters so that the DOS features are now in accordance with the literature data of Table III within the scatter of the data. Since we are mainly interested, however, in relative differences between the three amorphous structures and in a comparison of their density of states with that of graphite and diamond, we did not repeat the MD simulation of the structures with the new parameter set which gives the better results for graphite. In the spirit of our analysis it is only important to use the same calculation scheme for both amorphous and crystalline structures which was, of course, guaranteed.

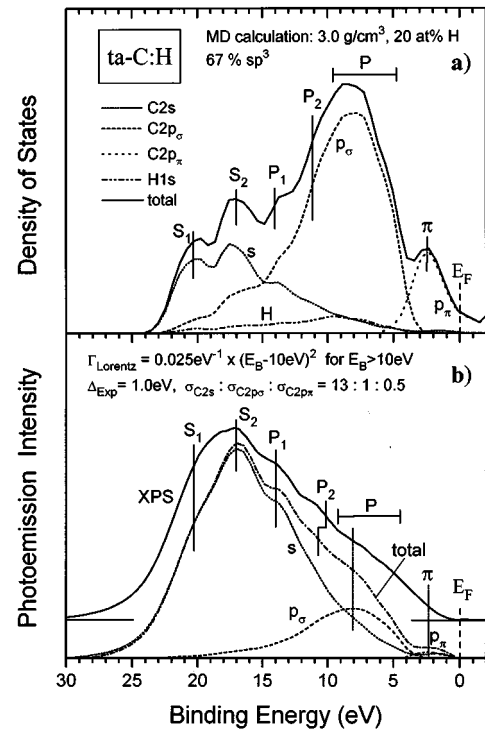


FIG. 6. (a) Partial and total DOS for amorphous hydrogenated carbon as obtained by simulated annealing MD. The hydrogen content of 20 at. % was in this case used as an additional input parameter to the mass density; an sp^3 content of 67% resulted. (b) XP spectrum of a *ta-C:H* sample and fit to the partial DOS analogous to Fig. 5(b).

Summarizing the results for graphite and diamond we conclude that our treatment of the DOS yields spectra which are in virtually perfect agreement with the measured XPS valence bands if one allows for an adjustment of the theoretical band energies. In this sense we expect a meaningful comparison between theory and experiment for the amorphous carbon modification as well. Naturally, the emphasis will be on the *s* parts of the PDOS due to their high photoemission cross sections at the photon energy employed here.

C. Results and discussion

In this section we will discuss the XP spectra of the three different amorphous carbon modifications in the same way as was done for diamond and graphite. Although we are conscious of the fact that the sharp DOS features of a crystalline material are, strictly speaking, due to van Hove singularities and thus rely on the periodicity of the atomic lattice, we will nevertheless show a number of striking similarities between the amorphous and the two crystalline materials investigated which demonstrate that nearest-neighbor or at least medium-range order in an amorphous material can still be sufficient to produce some of the characteristic features of the corresponding single-crystal DOS. We will demonstrate that the XP spectra significantly show the transition from an sp^3 -coordinated tetrahedral amorphous network in the case of *ta-C* to a structure with predominant sp^2 bonding in the case of *a-C:H*, the classical so-called “diamondlike” amorphous carbon. Figures 5 to 7 show the partial densities of

states as obtained by the molecular-dynamics calculation and the simulated valence-band spectra for *ta*-C, *ta*-C:H, and *a*-C:H. The experimental results for *ta*-C and *ta*-C:H are very similar but clearly different from those of *a*-C:H. The spectral features for *ta*-C:H are just slightly broader than for *ta*-C; the overall signature of the XP spectrum is, however, identical. For a systematic discussion we will use the partial DOS in Figs. 5–7(a) to identify those spectral features which are also resolved in the experiment. Starting with *ta*-C and *ta*-C:H [Figs. 5(a) and 6(a)], we have marked two peaks at 20.2 and 17.1 eV, S_1 and S_2 , respectively, indicating predominantly *s*-type character. Moreover, a distinct shoulder at 13.5 eV (in *ta*-C and slightly shifted to 14.0 eV in *ta*-C:H) and one indicated [more clearly in the DOS of *ta*-C:H in Fig. 6(a)] at around 11 eV can be seen and are labeled as P_1 and P_2 . Those four features are readily identified also in the experimental XP spectra [Figs. 6(b) and 7(b)]. The p_σ band appears in the XP spectra as one broad shoulder around 7 eV and is therefore just labeled P . Finally, the highest occupied states are formed by the π band which is—probably for the same reasons as in the case of graphite—not resolved in the XP spectra. Let us first consider peaks S_1 and S_2 in more detail. From the structural analysis of the calculated *ta*-C and *ta*-C:H models, we would expect similarities to diamond rather than graphite. Nevertheless, the sharp cutoff of the XP spectrum at the bottom of the valence bands [Figs. 5(b) and 6(b)] does resemble more that of graphite, which would indicate a considerable contribution of sp^2 hybridization within two-dimensional units. Those elements are, however, not found in a structural analysis of the *ta*-C and *ta*-C:H models. An alternative clue to the origin of the rather sharp cutoff in the XP spectra at high binding energy is provided by a theoretical investigation of the band structure of cubic and hexagonal diamond by Salehpour and Satpathy.⁴⁴ The latter form of carbon, called lonsdaleite, has been found to occur in meteorites⁵⁷ and has also been synthesized using extreme conditions of pressure and temperature.⁵⁸ Lonsdaleite is also fully tetrahedrally coordinated but with dihedral angles of 0° and 60°, in contrast to cubic diamond where it is always 60°. The characteristic difference in the *s* band of both materials is a splitting of the L'_2 maximum of the DOS of cubic diamond into two peaks with a spacing of 2.5 eV in lonsdaleite.⁴⁴ It is possibly the relaxation of the dihedral angle in the amorphous tetrahedral carbon modifications which causes a similar splitting as seen in lonsdaleite and thus the appearance of S_1 and S_2 . This is so far, however, only a working hypothesis and we have also found structures with almost identical ratios of staggered to eclipsed dihedral configurations which differ significantly with respect to the S_1 - S_2 splitting.

The second feature which confirms the structural similarity of the *ta*-C and *ta*-C:H samples with diamond is the appearance of the P_1 peak in the spectra at 13.5 eV, which resembles the L_1 maximum of diamond. The suppression of this peak when going to *a*-C:H [Fig. 7(b)] is the most sensitive signature for the structural change of the network. This suppression of P_1 relative to S_2 has its analogue in a similar asymmetry of the Q_{1u}^+ and Q_{1g}^+ maxima in graphite when compared to the approximate amplitudes of the van Hove singularities connected with L'_2 and L_1 in diamond. The

simulation also shows a shift of both P_1 by 1.9 eV and S_2 by 1.2 eV to higher binding energies. Although the experiment seems to confirm the shift of S_2 the contribution predicted as P_1 at 15.5 eV is missing in the XP spectrum.

As discussed in the last section for the case of graphite, our calculation tends to overestimate the binding energies in the σ bands of sp^2 -bonded material. We believe the same tendency holds for the DOS of the amorphous carbon. The true position of P_1 is thus more likely at a binding energy lower than 15.5 eV [Fig. 7(a)] and it will therefore contribute to the broad shoulder around 13 eV as indicated in the XP spectrum [Fig. 7(b)]. Finally, we discuss the P_2 peak. It is best resolved in the XP spectrum of *ta*-C:H at 10 eV and is somewhat broader in that of *ta*-C at 9.5 eV. A corresponding structure in the DOS [Figs. 5(a) and 6(a)] can be identified as a shoulder at around 10.5 eV. When going to *a*-C:H it shifts in the simulation as well as in the experiment to higher binding energies, i.e., to 12.4 eV, and merges with P_1 at 13.0 eV in the XP spectrum. Although this tendency is very well reproduced by the simulation we cannot identify corresponding features for P_2 in the DOS of graphite or diamond. Due to its lower binding energy as compared to S_1 , S_2 , and P_1 , however, P_2 will be of predominantly C 2*p* character and thus more sensitive to disorder due to the anisotropy of the *p* orbitals. Transferring characteristic features in the DOS of crystalline lattices to amorphous structures is certainly less significant in this case.

Considering finally the π band, we note the same discrepancy between experiment and fit as already discussed for graphite: while the calculation predicts a band clearly separated from the *s* bands, the experiment does not show a resolved structure for the π band. The reason for this difference lies probably in the same deficiencies of the calculation that have been discussed above for the case of graphite.

In conclusion, the *s*-type density of states of amorphous carbon which can be investigated by XPS proves to be sensitive to the structural properties of the material. A transition from tetrahedrally coordinated *ta*-C and *ta*-C:H to conventional *a*-C:H material with higher sp^2 content is visible by a characteristic XPS signature. An interesting feature in the DOS of tetrahedral amorphous carbon is a double peak in the *s*-type DOS at 17.1 and 20.2 eV, which is predicted by the calculation and confirmed by the XP spectra. Band-structure calculations of cubic and hexagonal diamond point towards a relaxation of the dihedral angle in the amorphous material as a reason for the splitting of the *s* band.

V. CORE-LEVEL ANALYSIS

In Fig. 8 we present the C 1*s* core-level spectra of the three amorphous samples and a single-crystal diamond. The position of the peaks is influenced by differences in both the C 1*s* ionization energy (“chemical shifts”) and the work function because photoemission binding energies in solids are always measured relative to the Fermi level. Since both effects cannot be separated no interpretation of changes in peak energies among different materials is possible without having a reliable common reference level. Besides different peak positions, however, also a change in the line shape between the various samples is apparent. The diamond line is only about half as wide (0.75 eV FWHM) as those of the

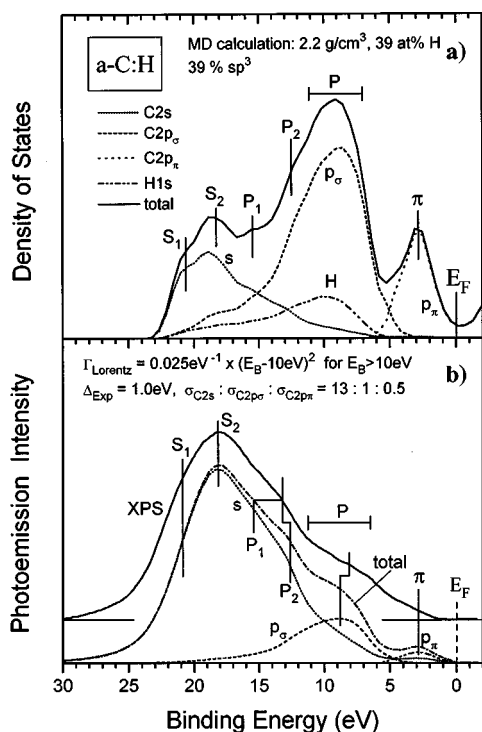


FIG. 7. (a) Partial and total DOS for amorphous hydrogenated carbon as obtained from MD. In contrast to Fig. 6, a higher hydrogen content of 40 at. % and a lower mass density of 2.2 g cm^{-3} were used as input parameters. The resulting structure revealed 67% sp^3 -coordinated carbon atoms. (b) XP spectrum of an *a*-C:H sample deposited by conventional RF plasma CVD and a fit to the partial DOS analogous to Fig. 5(b).

three amorphous samples (1.45 to 1.57 eV FWHM).

In an investigation of the diamond (111) surface the chemical shift of the C 1s binding energy on replacing one nearest carbon neighbor by hydrogen has been determined as $+0.5 \text{ eV}$.⁵⁹ In the case of the binary alloys *ta*-C:H and *a*-C:H, one possible source of the line broadening would thus be the chemical shift due to CH, CH₂, and CH₃ units in the material. However, *ta*-C without hydrogen has the broadest line; a different mechanism exists in the amorphous samples and is possibly also responsible for the line broadening in *ta*-C:H and *a*-C:H. Most likely, disorder-induced bonding-charge fluctuations, as they have already been identified in amorphous silicon,⁶⁰ are responsible. For the latter material, a more detailed analysis in order to separate chemical shift due to hydrogen and charge fluctuations could be performed because the hydrogen-induced effect was dominant. In the carbon case, however, the unhydrogenated material exhibits the broadest line and thus delivers no clue to the contribution of charge fluctuations to the broadening in the hydrogenated material. We therefore refrain from a quantitative analysis of the broadening mechanism.

On closer inspection the C 1s core line exhibits a clear asymmetry at the lower-binding-energy side. Also from experiments on clean single-crystal diamond (111) a surface core-level shift of -0.82 eV of the C 1s line has been established.⁵⁹ Although more specific structural properties of a surface reconstruction and relaxation also influence surface core-level shifts, we might as a zero-order approximation

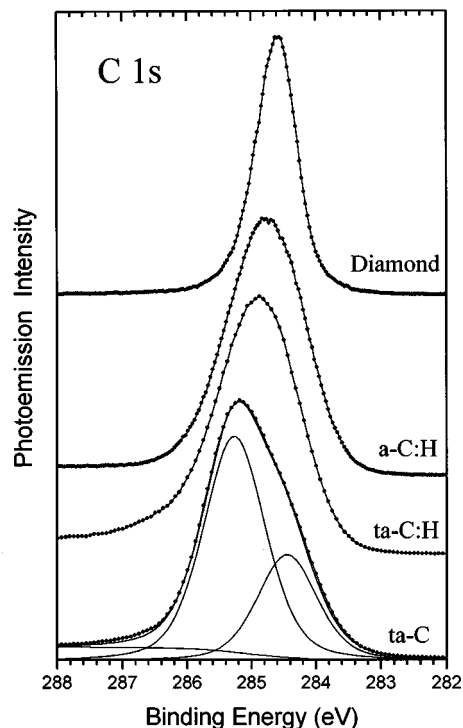


FIG. 8. C 1s core-level spectra of diamond and all three amorphous modifications investigated. The core line of diamond is smallest and is only determined by the lifetime broadening and the experimental resolution. The diamond was, after a hydrogenation, heated up to $800 \text{ }^\circ\text{C}$ and carries a monohydride termination and hence shows no surface core-level shift. The two hydrogen-containing samples, *a*-C:H and *ta*-C:H, show a much broader core line due to inhomogeneous broadening from the disordered network. Compared to the hydrogen-free *ta*-C, however, one finds that the hydrogen helps to relax network stress; in particular, bonding charge fluctuations that are responsible for the line broadening are less. The *ta*-C line appears to be composed of two components, ascribed to sp^2 and sp^3 phases as discussed in the text.

take this value as representative for threefold-coordinated carbon atoms. In the case of the *ta*-C they would correspond to sp^2 -hybridized carbon atoms mainly in π bonds. In fact, also in this respect the analogy to the clean (111) surface of diamond holds since the latter reconstructs in the form of π -bonded chains.⁶¹ As a working hypothesis we therefore ascribe the asymmetry on the low-energy side of the C 1s line in *ta*-C to sp^2 -coordinated carbon. A fit of the C 1s spectrum with two peaks separated by 0.82 eV in fact reveals an sp^2 -contribution of $31 \pm 4 \%$. This compares well to a value of 30% obtained from *K*-edge EELS.¹⁸

VI. SUMMARY

In this work we have analyzed the three presently available amorphous carbon materials that differ essentially by their way of manufacture. The samples have been analyzed by photoemission for their core levels as well as their valence bands. The C 1s core lines are approximately twice as wide for the three amorphous samples as for diamond, which we ascribe mainly to disorder-induced bonding charge fluctuations. In the case of the hydrogen-free *ta*-C we observe a

marked asymmetry on the low-binding-energy side, which is tentatively interpreted as due to sp^2 -coordinated carbon atoms. The valence-band spectra of both crystalline modifications could be consistently fitted to their partial densities of states using ratios of 13:1:0.5 for the $s:p_\sigma:p_\pi$ photoemission cross sections.

Peak positions in binding energy were well predicted from the calculation in the case of diamond but overestimated for graphite. Nevertheless, the characteristic changes

in the s -type and also in the p -type partial density of states (although less pronounced) between the three amorphous samples, which manifest themselves clearly in the XP valence-band spectra and which are due to different sp^2/sp^3 ratios, were correctly described by the calculation. The tetrahedrally coordinated amorphous network of the ta -C and ta -C:H samples shows a splitting of the s -band density of states which might be correlated with the relaxation of the dihedral angle in the disordered material.

- ¹F. A. Cotton and G. Wilkinson, *Advanced Inorganic Chemistry*, 4th ed. (Wiley, New York, 1980).
- ²P. Koidl, Ch. Wild, B. Dischler, J. Wagner, and M. Ramsteiner, in *Properties and Characterization of Amorphous Carbon Films*, edited by J. J. Pouch and S. A. Alterovitz, Materials Science Forum Vols. 52 and 53 (Transtech Publications, Switzerland, 1989), p. 41.
- ³M. Weiler, S. Sattel, K. Jung, H. Ehrhardt, V. S. Veerasamy, and J. Robertson, *Appl. Phys. Lett.* **64**, 2798 (1994).
- ⁴G. Jungnickel, M. Kühn, S. Deutschmann, F. Richter, U. Stephan, P. Blaudeck, and Th. Frauenheim, *Diam. Relat. Mater.* **3**, 1056 (1994).
- ⁵T. M. Burke, R. J. Newport, W. S. Howells, K. Gilkes, and P. Gaskell, *J. Non-Cryst. Solids* **164-166**, 1139 (1993).
- ⁶J. K. Walters, P. J. R. Honeybone, D. W. Huxley, R. J. Newport, and W. S. Howells, *J. Phys. Condens. Matter* **5**, L387 (1993).
- ⁷J. Fink, Th. Müller-Heinzerling, J. Pflüger, B. Scheerer, B. Dischler, P. Koidl, A. Bubenzer, and R. E. Sah, *Phys. Rev. B* **30**, 4713 (1984).
- ⁸M. A. Tamor, W. C. Vassell, and K. R. Carduner, *Appl. Phys. Lett.* **58**, 592 (1991).
- ⁹A. Grill, B. S. Meyerson, V. V. Patel, J. A. Reimer, and M. A. Petrich, *J. Appl. Phys.* **61**, 2874 (1987).
- ¹⁰B. Dischler, A. Bubenzer, and P. Koidl, *Solid State Commun.* **48**, 105 (1983).
- ¹¹A. Reyes-Mena, J. Gonzalez-Hernandez, R. Asomoza, and B. S. Chao, *J. Vac. Sci. Technol. A* **8**, 1509 (1990).
- ¹²A. Reyes-Mena, R. Asomoza, J. Gonzalez-Hernandez, and B. S. Chao, *J. Non-Cryst. Solids* **114**, 310 (1989).
- ¹³S. Xu, M. Hundhausen, J. Ristein, B. Yan, and L. Ley, *J. Non-Cryst. Solids* **164-166**, 1127 (1993).
- ¹⁴J. Schäfer, J. Ristein, and L. Ley, *Diam. Relat. Mater.* **3**, 861 (1994).
- ¹⁵P. Oelhafen, D. Ugolini, S. Schelz, and J. Eitle, in *Diamond and Diamondlike Films and Coatings*, edited by R. E. Clausing *et al.* (Plenum, New York, 1991), p. 377.
- ¹⁶J. Schäfer, J. Ristein, and L. Ley, *J. Non-Cryst. Solids* **164-166**, 1123 (1993).
- ¹⁷V. S. Veerasamy, Ph.D. thesis, University of Cambridge, 1994.
- ¹⁸V. S. Veerasamy, G. A. J. Amaratunga, W. I. Milne, P. Hewitt, P. J. Fallon, D. R. McKenzie, and C. A. Davis, *Diam. Relat. Mater.* **2**, 782 (1993).
- ¹⁹G. A. J. Amaratunga, V. S. Veerasamy, W. I. Milne, C. A. Davis, S. R. P. Silva, and H. S. MacKenzie, *Appl. Phys. Lett.* **63**, 370 (1993).
- ²⁰V. S. Veerasamy, G. A. J. Amaratunga, C. A. Davis, W. I. Milne, P. Hewitt, and M. Weiler, *Solid State Electron.* **37**, 319 (1994).
- ²¹V. S. Veerasamy, G. A. J. Amaratunga, W. I. Milne, J. Robertson, and P. J. Fallon, *J. Non-Cryst. Solids* **164-166**, 1111 (1993).
- ²²J.-J. Yeh, *Atomic Calculation of Photoionization Cross-Sections and Asymmetry Parameters* (Gordon and Breach, Longhorne, 1993).
- ²³P. Steiner, H. Höchst, and S. Hüfner, in *Photoemission in Solids II*, edited by L. Ley and M. Cardona, Topics in Applied Physics Vol. 27 (Springer, Berlin, 1979), p. 349.
- ²⁴M. Weiler, S. Sattel, K. Jung, H. Ehrhardt, and V. S. Veerasamy, *Diam. Relat. Mater.* **3**, 608 (1994).
- ²⁵M. Weiler, R. Kleber, S. Sattel, K. Jung, H. Ehrhardt, G. Jungnickel, S. Deutschmann, U. Stephan, P. Blaudeck, and Th. Frauenheim, *Diam. Relat. Mater.* **3**, 245 (1994).
- ²⁶When $n_{\text{diam}}=2.4$ and $n_h=0.53$ denote the contributions of the four valence electrons of a carbon atom in diamond and that of the valence electron of hydrogen, respectively, to the UPS spectral region investigated in Ref. 16, and the average photoemission cross sections are σ_c for carbon and σ_h for hydrogen valence electrons, the relative contribution γ of hydrogen to the spectrum is given by $\gamma=n_h\sigma_h/(n_{\text{diam}}\sigma_c)$. With that correction the sp^2 content resulting from the UPS analysis increases by a factor $[1-p(1-\gamma)]/(1-p)$, where p is the hydrogen content of the sample (0.4 in our case). If, as a rough approximation, the atomic photoionization cross sections for $\sigma_{\text{H}1s}=1.884$, $\sigma_{\text{C}2s}=1.230$, and $\sigma_{\text{C}2p}=6.121$ (Mb/subshell) are used in conjunction with the calculated densities of states for diamond and a -C:H [Figs. 3(a) and 7(a)] the ratio γ can be estimated to be about 0.9 and the sp^3 content is reduced to 56%.
- ²⁷E. A. Taft and H. R. Philipp, *Phys. Rev.* **138**, A197 (1965).
- ²⁸J. Daniels, C. v. Festenberg, H. Raether, and K. Zeppenfeld, in *Springer Tracts in Modern Physics* (Springer, Berlin, 1970), Vol. 54, p. 77.
- ²⁹H. Raether, *Excitation of Plasmons and Interband Transitions by Electrons* (Springer, New York, 1980).
- ³⁰P. G. Lurie and J. M. Wilson, *Surf. Sci.* **65**, 476 (1977).
- ³¹O. M. Küttel, L. Diederich, E. Schaller, O. Carnal, and L. Schlappbach, *Surf. Sci.* **337**, L812 (1995).
- ³²Th. Frauenheim, P. Blaudeck, U. Stephan, and G. Jungnickel, *Phys. Rev. B* **48**, 4823 (1993).
- ³³Th. Frauenheim, U. Stephan, P. Blaudeck, and G. Jungnickel, *Diam. Relat. Mater.* **3**, 462 (1994).
- ³⁴U. Stephan, Th. Frauenheim, P. Blaudeck, and G. Jungnickel, *Phys. Rev. B* **50**, 1482 (1994).
- ³⁵J. H. Scofield, *J. Electron Spectrosc.* **8**, 129 (1976).
- ³⁶U. Gelius, in *Electron Spectroscopy*, edited by D. A. Shirley (North-Holland, Amsterdam, 1972), p. 311.
- ³⁷J. E. Inglesfield and E. W. Plummer, in *Angle-Resolved Photoemission*, edited by S. D. Kevan, Studies in Surface Science and Catalysis Vol. 74 (Elsevier, Amsterdam, 1992).

- ³⁸E. O. Kane, *Phys. Rev.* **159**, 624 (1967).
- ³⁹A. Zunger and A. J. Freeman, *Phys. Rev. B* **15**, 5049 (1977).
- ⁴⁰G. B. Bachelet, H. S. Greenside, G. A. Baraff, and M. Schlüter, *Phys. Rev. B* **24**, 4745 (1981).
- ⁴¹J. R. Chelikowsky and S. G. Louie, *Phys. Rev. B* **29**, 3470 (1984).
- ⁴²M.-Z. Huang and W. Y. Ching, *Phys. Chem. Solids* **46**, 977 (1985).
- ⁴³S. Fahy, S. G. Louie, and M. L. Cohen, *Phys. Rev. B* **34**, 1191 (1986).
- ⁴⁴M. R. Salehpour and S. Satpathy, *Phys. Rev. B* **41**, 3048 (1990).
- ⁴⁵F. J. Himpsel, J. F. van der Veen, and D. E. Eastman, *Phys. Rev. B* **22**, 1967 (1980).
- ⁴⁶A. Zunger, *Phys. Rev. B* **17**, 626 (1978).
- ⁴⁷L. Samuelson and I. P. Batra, *J. Phys. C* **13**, 5105 (1980).
- ⁴⁸J.-C. Charlier, X. Gonze, and J.-P. Michenaud, *Phys. Rev. B* **43**, 4579 (1991).
- ⁴⁹R. F. Willis, B. Fitton, and G. S. Painter, *Phys. Rev. B* **9**, 1926 (1974).
- ⁵⁰R. C. Tatar and S. Rabii, *Phys. Rev. B* **25**, 4126 (1982).
- ⁵¹N. A. W. Holzwarth, S. G. Louie, and S. Rabii, *Phys. Rev. B* **26**, 5382 (1982).
- ⁵²H. J. F. Jansen and A. J. Freeman, *Phys. Rev. B* **35**, 8207 (1987).
- ⁵³F. R. McFeely, S. P. Kowalczyk, L. Ley, R. G. Cavell, R. A. Pollak, and D. A. Shirley, *Phys. Rev. B* **9**, 5268 (1974).
- ⁵⁴A. Bianconi, S. B. M. Hagström, and R. Z. Bachrach, *Phys. Rev. B* **16**, 5543 (1977).
- ⁵⁵I. T. McGovern, W. Eberhardt, E. W. Plummer, and J. E. Fischer, *Physica B+C* **99B**, 415 (1980).
- ⁵⁶A. R. Law, J. J. Barry, and H. P. Hughes, *Phys. Rev. B* **28**, 5332 (1983).
- ⁵⁷R. E. Hanneman, H. M. Strong, and F. B. Bundy, *Science* **155**, 955 (1987).
- ⁵⁸F. P. Bundy and J. S. Kasper, *J. Chem. Phys.* **46**, 4737 (1967).
- ⁵⁹R. Graupner, J. Ristein, and L. Ley, *Surf. Sci.* **320**, 201 (1994).
- ⁶⁰L. Ley, J. Reichardt, and R. L. Johnson, *Phys. Rev. Lett.* **49**, 1664 (1982).
- ⁶¹K. C. Pandey, *Phys. Rev. Lett.* **49**, 223 (1982).